Scripta Materialia 201 (2021) 113952

Contents lists available at ScienceDirect

Scripta Materialia

journal homepage: www.elsevier.com/locate/scriptamat

Remelting induced fully-equiaxed microstructures with anomalous eutectics in the additive manufactured $Ni_{32}Co_{30}Cr_{10}Fe_{10}Al_{18}$ eutectic high-entropy alloy

Kexuan Zhou, Junjie Li*, Qingfeng Wu, Zhilin Zhang, Zhijun Wang*, Jincheng Wang

State Key Laboratory of Solidification Processing, Northwestern Polytechnical University, Xi'an 710072, China

ARTICLE INFO

Article history:
Received 4 March 2021
Revised 16 April 2021
Accepted 18 April 2021

Keywords:
Eutectic high-entropy alloys
Additive manufacturing
Anomalous eutectics
Laser remelting
Columnar-to-equiaxed transition

ABSTRACT

Large columnar grains with epitaxial growth are commonly obtained in the additive manufacturing of alloys, resulting in anisotropic mechanical properties and even hot-tearing cracks. Here, we demonstrate a new approach via remelting-introduced columnar-to-equiaxed transformation to promote the formation of fully-equiaxed microstructures in the additive manufacturing of $Ni_{32}Co_{30}Cr_{10}Fe_{10}Al_{18}$ eutectic high-entropy alloy. Our present work displays promising isotropic mechanical properties with a superior combination of strength and ductility, compared to conventional as-cast and other as-printed eutectic high-entropy alloys. This novel finding could be applicable to the additive manufacturing of other eutectic systems for equiaxed microstructure control and performance optimization.

Additive manufacturing (AM), possessing high-level control and rapid solidification rates during the manufacturing process, is a promising technology for the production of complex, three-dimension parts with optimized performance [1–8]. Due to its intrinsic high cooling rate and high thermal gradient and layer-by-layer deposition process, large columnar grains with epitaxial growth are commonly obtained in the additive manufacturing of alloys [9]. However, the columnar growth of dendrites in AM is undesirable for the majority of alloys, which may result not only in anisotropic mechanical properties but also in hot-tearing cracks due to the volumetric solidification shrinkage and thermal contraction [10]. Columnar-to-equiaxed transition (CET) in AM of alloys has been paid constant attention to for achieving equiaxed fine-grained microstructures without cracking and optimized mechanical properties [10–13]. Attempts to achieve CET under rapid solidification of AM process can be mainly divided into three strategies: (i) adjusting the intrinsic and extrinsic processing parameters, such as controlling processing parameters like laser power, scanning speed, etc. for the low temperature gradient and high solidification velocity or applying high-intensity ultrasound to further obtain fully equiaxed microstructures [12,13]; (ii) introducing suitable nucleation particles directly to facilitate heterogeneous nucleation and equiaxed grain growth [10]; (iii) adding solute elements with high growth restriction factor for extending the constitutional supercooling zone and promoting more nucleation [11].

However, it is still an open question whether there is another method to achieve CET in AM. Intriguingly, the rapid solidification of eutectic alloys involving remelting process provides a promising way for CET. Lin et al. [14] reported the formation of an uncoupled anomalous eutectics layer at the bottom of the molten pool, resulted from partially remelting and broken of α-Ni primary phase in laser remelting of the near-eutectic Ni-Sn alloy. Recently, G. Requena et al. [15] combined phase-field modeling and experimental observations to investigate the Fe-Fe_2Ti eutectic microstructures obtained by direct laser deposition (DLD), revealing that anomalous eutectics formed at the interlayer boundaries resulted from nucleation on partially remelted and spherodized lamellae as seed particles. However, there is only a narrow layer formed with these unique structures. Inspired by this partially remelting phenomenon, it is quite interesting whether the remelted microstructures from the previously deposited layer can be controlled as the in-situ nucleation sites to achieve fully-equiaxed microstructures in AM-fabricated eutectic alloys.

To this end, we here investigated a eutectic high-entropy alloy (EHEA) fabricated via DLD, by focusing on the remelting behavior and its evolution. A new mechanism to induce equiaxed microstructures in AM was found. Experimental findings characterized by electron backscatter diffraction (EBSD) provided detailed insights into the microstructure evolution of the as-deposited EHEA and the underlying mechanism. It is worth mentioning that

* Corresponding authors.
E-mail addresses: lijunjie@nwpu.edu.cn (J. Li), zhjwang@nwpu.edu.cn (Z. Wang).

https://doi.org/10.1016/j.scriptamat.2021.113952
1359-6462/

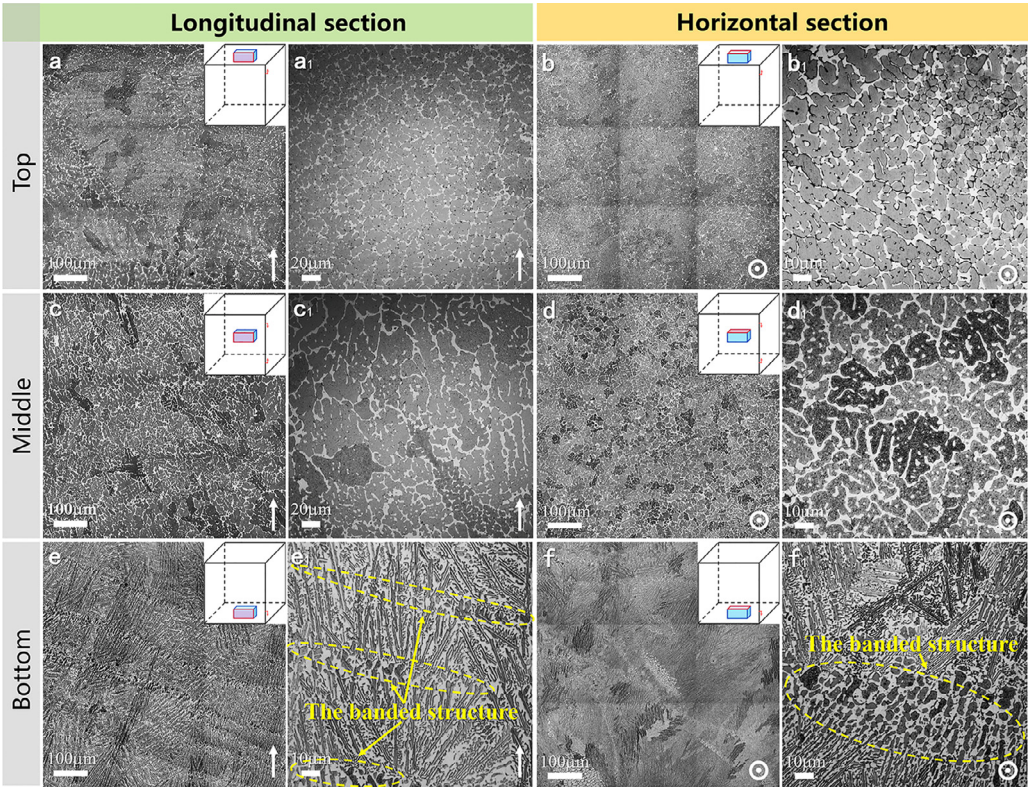

Fig. 1. Microstructural analyses of the as-deposited $Ni_{32}Co_{30}Cr_{10}Fe_{10}Al_{18}$ EHEA via optical microscopy: (a, a_1, b, b_1) anomalous eutectics at the top; (c, c_1, d, d_1) anomalous eutectics in the middle; (e, e_1, f, f_1) eutectic structures and the banded structures with anomalous eutectics at the bottom.

EHEA is chosen based on its excellent mechanical properties with the compatibility of strength and ductility as well as its good castability, which has emerged as a leading edge of metallic materials researches [16–20].

The $Ni_{32}Co_{30}Cr_{10}Fe_{10}Al_{18}$ (at. %) EHEA [21,22] was chosen in our present work. The cube-shape samples with dimensions of 12 × 12 × 12 mm^3 were manufactured from the ball-milling mixed EHEA powders using a DLD system equipped with a 4 kW continuous-wave CO_2 laser. The processing parameters including a laser power of 1500 W, a laser spot diameter of 1.5 mm, three scanning velocities of 1.8, 2.7, and 3.6 mm/s, two powder feed rates of 1.908 kg/h and 1.507 kg/h, a lifting distance of 0.15 mm, the overlap rate of 50 %, and the bi-directional deposition pattern were applied. It should be noted that low scanning speeds were chosen based on the consideration of that propitious to remelting. The specimens with different processing parameters are numbered and listed in Table S1 and the detailed microstructure analyses were mainly carried out on the sample P2. The as-deposited specimens were cut and then polished along the building direction and vertical to the building direction for observation, respectively. Microstructure characterizations were observed via optical microscopy (OM, Olympus P4000). Backscattered electron (BSE) imaging, energy dispersive spectrometry (EDS) mapping analysis, and EBSD were carried out on a TESCAN MIRA3 at 20 kV voltage. XRD analyses were performed using an X-ray diffractometer (Shimadzu, MAXima XRD-7000) with Cu Kα radiation at a scanning rate of 5° min^{-1}, and a 2θ angle ranging from 20° to 100°. In-situ observation of the remelting process was conducted via a high-temperature laser scanning confocal microscope (HTLSCM, VL2000DX-SVF18SP) under the protection of a high-purity Ar atmosphere. The as-cast counterpart prepared by arc melting and copper mold casting was cut for the HTLSCM experiment. Compression testing was carried out on ∅ 3 × 5 mm samples at room temperature using a materials testing machine (INSTRON 3382) with a strain rate of 1 × 10^{-3} s^{-1}. Longitudinal and horizontal samples were cut by an electrical discharge wire-cutting machine, respectively. The long axis of longitudinal samples is parallel to the building direction, while that of horizontal samples is vertical to the building direction.

Fig. 1 presented the representative optical micrographs of the as-deposited $Ni_{32}Co_{30}Cr_{10}Fe_{10}Al_{18}$ EHEA at different positions from the longitudinal and cross-sectional views, as indicated by the inset of Figs. 1a-1f (referring to the corresponding position and surface). At the bottom, typical melting pool morphologies with banded structures were observed, as shown in Figs. 1e and 1f. The amplified microstructures in Figs. 1e_1 and 1f_1 showed the crosslinked skeleton-like structure and granulated structure in the banded zones (highlighted in yellow circles). These structures are similar to the anomalous eutectic structures (AES) reported in the previous eutectic alloys fabricated by laser remelting or AM [14,15,23,24]. The microstructures between the banded zones exhibited regular lamellae eutectic structures (ES). The banded structures are only exhibited in the bottom region. With the increasing deposition height, there are no hemispherical melt-pool features, as shown in Figs. 1a-1d. Instead, microstructures at high magnification, as shown in Figs. 1a_1-1d_1, exhibited the fully anomalous eutectic structures. Compared with the microstructures at the top region, the coarse anomalous eutectics were obtained and there were micron-grade particles distributed in the dendritic-like B2 matrix in the middle zone. The overall longitudinal sectional microstructures are shown in Fig. S1 in **Supplementary Information,** indicating the evident microstructure evolution from bottom to top. Additionally, the optical micrographs of the other as-deposited EHEAs (P1, P3, and P4) along the building direc-

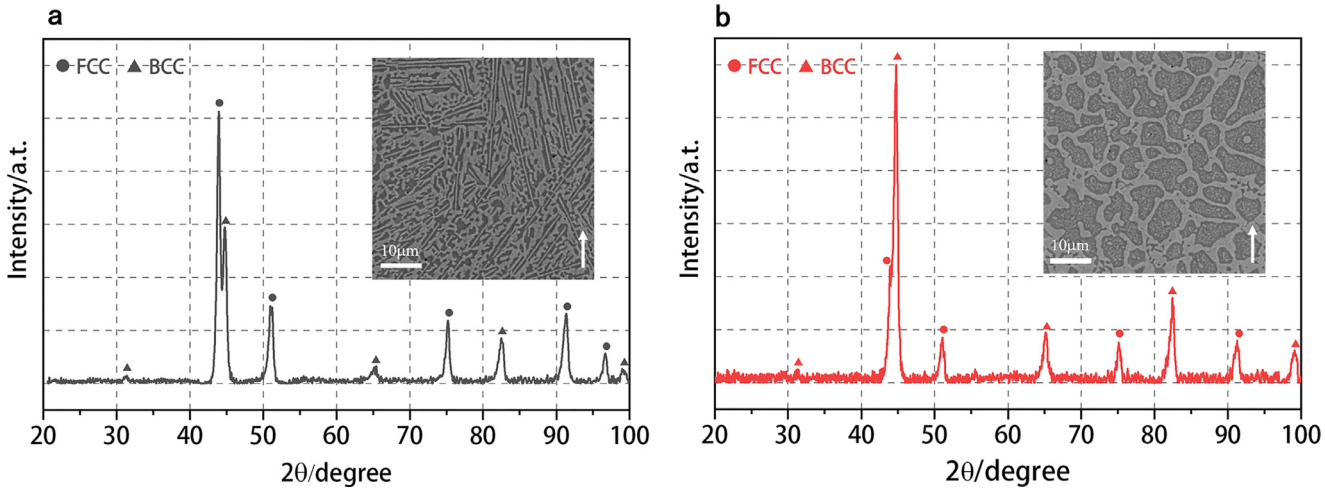

Fig. 2. Phase constitutions for the as-deposited $Ni_{32}Co_{30}Cr_{10}Fe_{10}Al_{18}$ EHEA at different zones: (a) eutectic structure zone and (b) anomalous eutectic zone.

tion are shown in Fig. S2, in which the fully AES formed as well.

The phase constitution in the as-deposited $Ni_{32}Co_{30}Cr_{10}Fe_{10}Al_{18}$ EHEA was further clarified by XRD, as shown in Fig. 2. An FCC-B2 dual-phase constitution both in the eutectic and anomalous eutectic zones was confirmed, which is consistent with the as-cast counterpart [21]. The overall composition of representative eutectic and anomalous eutectic zones of the as-deposited EHEA was measured respectively by EDS mapping, as listed in Table S2, indicating the compositional consistency after the deposition. The corresponding elemental distribution maps were shown in Fig. S3. These results demonstrated the similar phase constitution and chemical composition in regions of eutectics and anomalous eutectics, and the microstructure evolution from eutectic structures to anomalous eutectics should be highly dependent on the solidification process.

EBSD results of different positions in the as-deposited EHEA were shown in Fig. 3. As seen in the corresponding inverse pole figures (IPFs) of Figs. 3a-d, the orientation of grains in different positions showed a significant difference. There is a transition from aligned dendritic eutectic structures with the banded structures to anomalous eutectics with random orientations. At the bottom, it can be seen that the regular eutectic structures exhibited consistent orientations with the interlayer anomalous eutectics. As the increase of deposition height, at the transformation zone of dendritic eutectics to fully anomalous eutectics, the orientations of the skeleton-like FCC phases in anomalous eutectics were consistent with FCC phases in the lamellae, while the dendritic B2 phase in anomalous eutectics exhibited random orientations. As the further increase of deposition height, both FCC and B2 phases in anomalous eutectics exhibited random crystallographic orientations, presenting fully-equiaxed microstructures.

As seen in the phase map of Fig. 3a and b, there is a Kurdjumov-Sach (K-S) orientation relationship (highlighted in blue) between the FCC and B2 phases in the bottom as-deposited microstructures, not only in the regular eutectics but also in the interlayer anomalous eutectics, indicating the coupled growth of these two eutectic phases. However, with the increase of deposition height, there is no longer maintaining the K-S orientation relationship in the fully anomalous eutectics, indicating the decoupled growth of the eutectic phase during the laser deposition. Interestingly, small particles distributed in the dendritic-like B2 matrix maintain the K-S orientation relationship (highlighted in blue) with the matrix phase, indicating these particles precipitated due to the later cyclic heat treatment during deposition. In addition, it seems that the volume fraction of the B2 phase increases in the fully anomalous eutectic region. Previous research [20,25] had confirmed that the microstructure morphology (involving phase composition and phase volume fraction) of eutectic alloys is sensitively affected by solidification conditions, especially under non-equilibrium solidification.

The formation mechanism of the banded anomalous FCC+B2 eutectics at the bottom region is similar to the previous related researches [14,15], resulting from the nucleation on the partially remelted primary structures. The regular dendritic eutectics formed at the beginning of the DLD since the introduced heat fast dissipated through the substrate. During the subsequent laser scanning process, the FCC lamellae with a low melting point tended to melt into the liquid while the NiAl-riched B2 lamellae partially melted and tended to transform into granules. This partially remelting phenomenon of primary lamellae eutectics was commonly observed and reported in eutectic alloys with phase composition consisting of solid-solution phase [26–28]. In the following rapid solidification, the liquid phase solidified between regions of the granulated B2 phase, resulting in the anomalous banded structure formation. The consistent K-S relationship and orientations between the banded anomalous eutectics and regular eutectics indicated the epitaxial growth of lamellae eutectics originating from the anomalous eutectics ahead.

However, with the increase of deposition height, the growth of the FCC+B2 eutectic changed to anomalous eutectics with random orientations. One of the possible reasons is the varied heat dissipation. As the deposition goes on, the thermal accumulation would result in a reduced temperature gradient and increased molten pool size. As the depth of the molten pool increased, the remelting zone increased, where the more FCC and B2 phases in primary lamellae eutectics dissolved. The B2 phase with a higher melting point will dissolve slower than the FCC phase, and the B2 skeleton will be fragmented due to the flow in the molten pool. The delayed melting of the B2 phase was further confirmed in the in-situ remelting observation of the regular lamellae eutectic $Ni_{32}Co_{30}Cr_{10}Fe_{10}Al_{18}$ EHEA, as shown in Fig. S4 and Video S1. It can be seen that as the temperature approaches the melting point, the white FCC lamellae phase remelts and rapidly propagates, while the dark B2 phase remains solid and flow in the FCC melt. Then, during the deposition of the next layer, the B2 fragmentations will grow individually in the molten pool, suppressing the epitax-

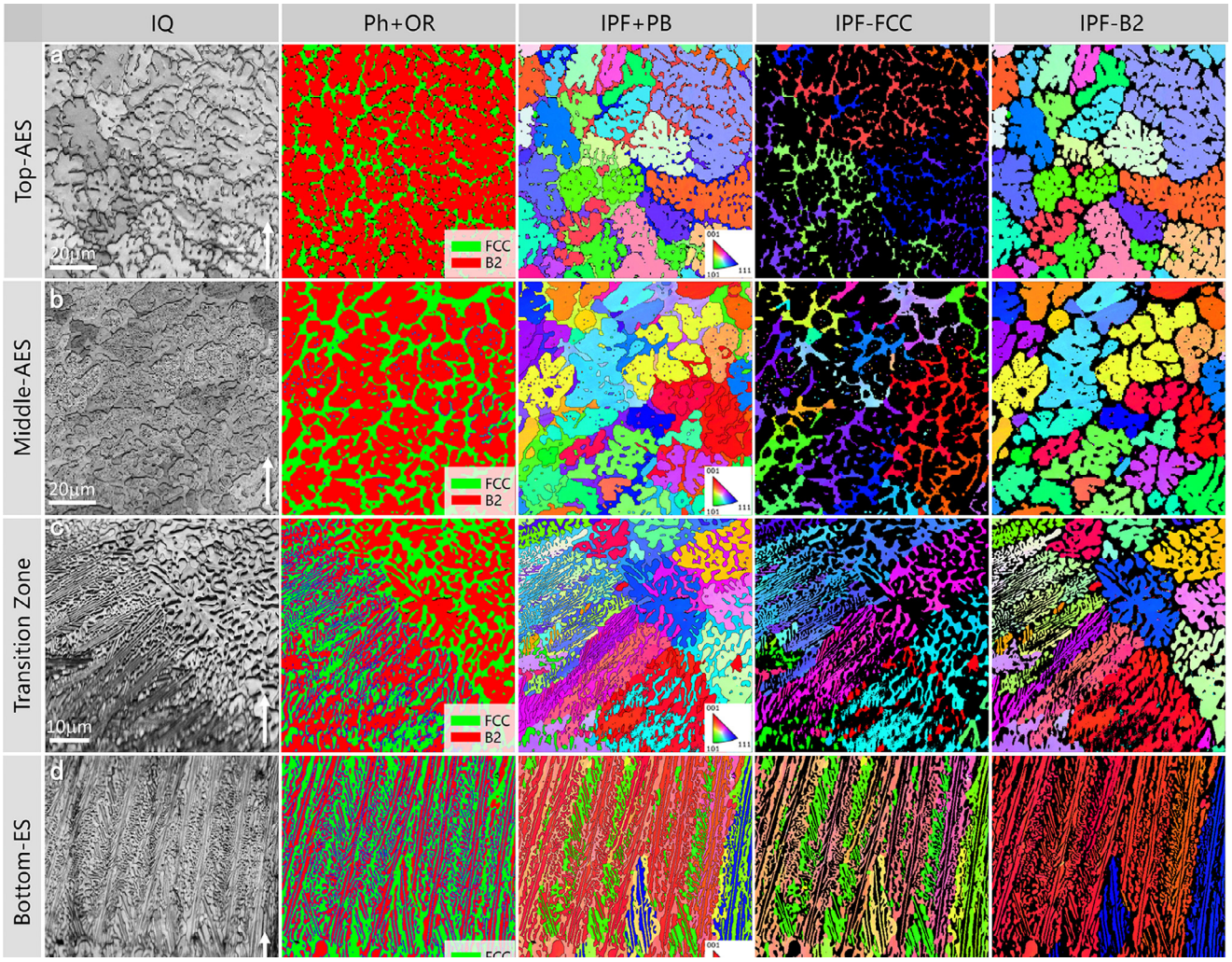

Fig. 3. EBSD analyses of representative microstructures in the as-deposited $Ni_{32}Co_{30}Cr_{10}Fe_{10}Al_{18}$ EHEA: (a) the anomalous eutectic zone at the top; (b) the anomalous eutectic zone in the middle; (c) the transformation zone from dendritic eutectic structures to fully anomalous eutectic structures; and (d) the regular eutectic zone at the bottom. (IQ: image quality; Ph: phase; OR: orientation relationship; IPF: inverse pole figure; PB: phase boundary)

ial lamellae growth. The FCC phase will nucleate upon the remnants B2 or epitaxially growth from the previous layer. As shown in Fig. 3, the transition layer indicated that the FCC phase exhibited consistent orientations with the frontier lamellae FCC phase while the B2 phase showed the new random orientations.

Notably, columnar grains with epitaxial growth in additively manufactured alloys result in anisotropic mechanical properties. The obtaining of fully-equiaxed microstructures in our work, as shown in Fig. 4a, would significantly affect and improve this undesirable asymmetric mechanical performance. Compressive tests were performed on the as-deposited EHEA specimens fabricated via different parameters as shown in Fig. 4b, where the inset plots present the way compressed samples were cut. The corresponding results of compressive performance are summarized in Table S3. Comparing the compressive performance of the same as-deposited specimen under different loading directions, the isotropic mechanical properties were achieved owing to the obtaining of fully-equiaxed anomalous eutectic structures. Meanwhile, comparing the as-deposited specimens with different processing parameters, similar ductilities were obtained, while higher strength was attained with lower scanning speed. The optimum performance in our present work exhibited a high compression strength of ~3.2 GPa and a fracture strain of ~ 45%. As shown in Fig. 4c, the as-deposited EHEAs with fully-equiaxed anomalous eutectics display a superior combination of strength and ductility, compared with the previously reported as-cast EHEAs [29–41] and the AM-fabricated EHEA [42] (listed in Table S4). This may result from the excellent synergistic deformation between ductile FCC and hard B2 phase as well as BCC-FCC interfacial effects [43,44]. Furthermore, the properties of as-deposited $Ni_{32}Co_{30}Cr_{10}Fe_{10}Al_{18}$ EHEAs are also superior to that of AM-fabricated Al-Co-Cr-Fe-Ni HEAs [45,46] because of the excellent microstructures as well as good printability.

In conclusion, the present work has demonstrated a new approach to promote the formation of fully-equiaxed microstructures in AM via remelting-introduced CET during the deposition. The EBSD results indicated that in the AM of $Ni_{32}Co_{30}Cr_{10}Fe_{10}Al_{18}$ EHEA, the high-melting-point B2 phase partially remelted and remained as in-situ nucleation sites facilitate equiaxed grain growth, while the FCC phase remelted into the liquid during the next layer deposition. Excellent isotropic mechanical properties were achieved with equiaxed grains. This work demonstrates the potential of manipulating the laser remelting process of AM of eutectic alloys to adjust the as-deposited microstructures achieving CET and optimizing mechanical properties.

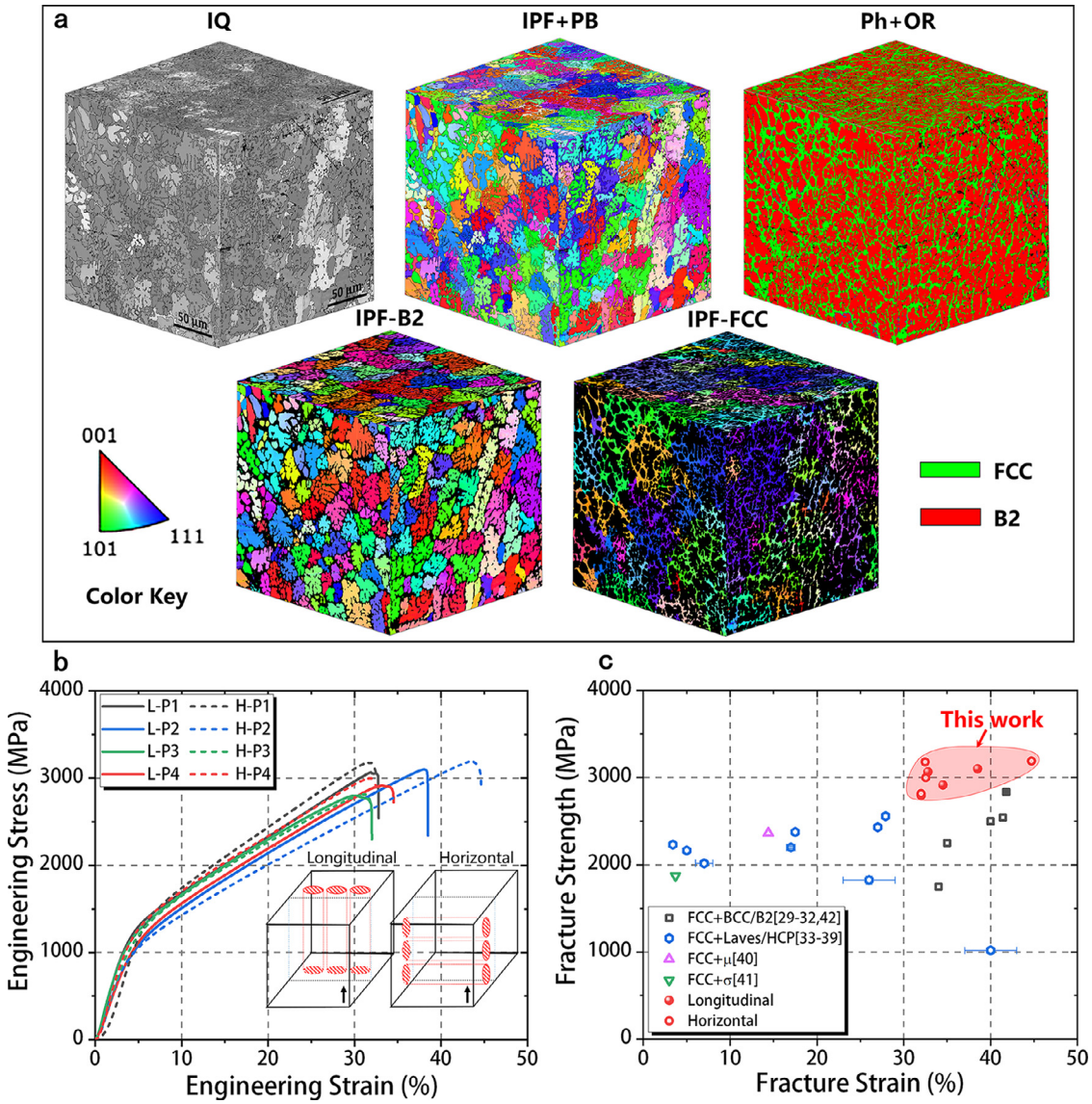

Fig. 4. (a) EBSD maps in views from different directions of the as-deposited $Ni_{32}Co_{30}Cr_{10}Fe_{10}Al_{18}$ EHEA, demonstrating the obtained fully-equiaxed structure. (b) Representative compressive engineering strain-stress curves of the as-deposited EHEAs fabricated via different processing parameters in this work; solid lines indicate longitudinal samples, while dotted lines indicate horizontal samples. (c) The comparison of the compressive performance of the previously reported EHEAs [29-42] and our work.

Declaration of Competing Interest

The authors declare that they have no known competing financial interests or personal relationships that could have appeared to influence the work reported in this paper.

Acknowledgments

The work was financially supported by the National Key R&D Program of China (No. 2018YFB1106003) and the Fund of SKLSP in NWPU (No. 03-TS-2019).

Supplementary materials

Supplementary material associated with this article can be found, in the online version, at doi:10.1016/j.scriptamat.2021.113952.

References

[1] C. Han, Q. Fang, Y. Shi, S.B. Tor, C.K. Chua, K. Zhou, Adv. Mater. (2020) e1903855.
[2] N. Li, S. Huang, G. Zhang, R. Qin, W. Liu, H. Xiong, G. Shi, J. Blackburn, J. Mater. Sci. Technol. 35 (2) (2019) 242–269.
[3] T. DebRoy, H.L. Wei, J.S. Zuback, T. Mukherjee, J.W. Elmer, J.O. Milewski, A.M. Beese, A. Wilson-Heid, A. De, W. Zhang, Prog. Mater Sci. 92 (2018) 112–224.
[4] D. Herzog, V. Seyda, E. Wycisk, C. Emmelmann, Acta Mater. 117 (2016) 371–392.
[5] S.M. Thompson, L. Bian, N. Shamsaei, A. Yadollahi, Add. Manufac. 8 (2015) 36–62.
[6] N. Shamsaei, A. Yadollahi, L. Bian, S.M. Thompson, Add. Manufac. 8 (2015) 12–35.
[7] A.O. Moghaddam, N.A. Shaburova, M.N. Samodurova, A. Abdollahzadeh, E.A. Trofimov, J. Mater. Sci. Technol. (2020).
[8] W.-C. Lin, Y.-J. Chang, T.-H. Hsu, S. Gorsse, F. Sun, T. Furuhara, A.-C. Yeh, Add. Manufac. (2020).
[9] Y. Kok, X.P. Tan, P. Wang, M.L.S. Nai, N.H. Loh, E. Liu, S.B Tor, Mater. Des. 139 (2018) 565–586.
[10] J.H. Martin, B.D. Yahata, J.M. Hundley, J.A. Mayer, T.A. Schaedler, T.M. Pollock, Nature 549 (7672) (2017) 365–369.
[11] D. Zhang, D.H. StJohn, D. Qiu, M.A. Easton, M.A. Gibson, Nature 576 (7785) (2019) 91–95.

[12] C.J. Todaro, M.A. Easton, D. Qiu, D. Zhang, M.J. Bermingham, E.W. Lui, M. Brandt, D.H. StJohn, M. Qian, Nat. Commun. 11 (1) (2020) 142.
[13] J. Zhang, Y. Liu, M. Bayat, Q. Tan, Y. Yin, Z. Fan, S. Liu, J.H. Hattel, M. Dargusch, M.-X. Zhang, Scr. Mater. 191 (2021) 155–160.
[14] X. Lin, Y.-Q. Cao, Z.-T. Wang, J. Cao, L.-L. Wang, W.-D. Huang, Acta Mater. 126 (2017) 210–220.
[15] G. Requena, K. Bugelnig, F. Sket, S. Milenkovic, G. Rödler, A. Weisheit, J. Gussone, J. Haubrich, P. Barriobero-Vila, T. Pusztai, L. Gránásy, A. Theofilatos, J.C.d. Silva, U. Hecht, Add. Manufac. (2020) 33.
[16] I. Baker, M. Wu, Z. Wang, Mater. Charact. 147 (2019) 545–557.
[17] Y. Lu, Y. Dong, H. Jiang, Z. Wang, Z. Cao, S. Guo, T. Wang, T. Li, P.K. Liaw, Scr. Mater. 187 (2020) 202–209.
[18] R.J. Vikram, B.S. Murty, D. Fabijanic, S. Suwas, J. Alloys Compd. (2020).
[19] J. Joseph, M. Imran, P.D. Hodgson, M.R. Barnett, D.M. Fabijanic, Manufac. Lett. (2020).
[20] V. Ocelík, N. Janssen, S.N. Smith, J.T.D. Hosson, Jom 68 (7) (2016) 1810–1818.
[21] Q. Wu, Z. Wang, X. Hu, T. Zheng, Z. Yang, F. He, J. Li, J. Wang, Acta Mater. 182 (2020) 278–286.
[22] Z. Yang, Z. Wang, Q. Wu, T. Zheng, P. Zhao, J. Zhao, J. Chen, Appl. Phys. A 125 (3) (2019).
[23] R. Zhao, J. Gao, H. Liao, N. Fenineche, C. Coddet, Add. Manufac., 2020.
[24] Z. Wang, X. Lin, Y. Cao, W. Huang, J. Alloys Compd. 577 (2013) 309–314.
[25] L. Wang, C. Yao, J. Shen, Y. Zhang, T. Wang, Y. Ge, L. Gao, G. Zhang, Intermetallics (2020) 118.
[26] X.X. Wei, X. Lin, Q.S.Huang W.Xu, M. Ferry, J.F. Li, Y.H. Zhou, Acta Mater. 95 (2015) 44–56.
[27] L.J. Liu, X.X.Wei M. Ferry, J.F Li, Scr. Mater. 174 (2020) 72–76.
[28] H. Dong, Y.Z. Chen, K. Wang, G.B. Shan, Z.R. Zhang, K. Huang, F. Liu, Scr. Mater. 177 (2020) 123–127.
[29] Y. Dong, Y. Lu, J. Mater. Eng. Perform. 27 (1) (2017) 109–115.
[30] Xiangli Hu, D. Chen, J. Mater. Eng. Perform. 27 (7) (2018) 3566–3573.
[31] Y. Dong, Z. Yao, X. Huang, F. Du, C. Li, A. Chen, F. Wu, Y. Cheng, Z. Zhang, J. Alloys Compd. 823 (2020).
[32] X. Huang, Y. Hu, Z. Wu, Y. Dong, C. Li, Y. Cheng, Z. Zhang, Mater. Sci. Forum 993 (2020) 281–286.
[33] L. Jiang, Y. Lu, W. Wu, Z. Cao, T. Li, J. Mater. Sci. Technol. 32 (3) (2016) 245–250.
[34] H. Jiang, L. Jiang, D. Qiao, Y. Lu, T. Wang, Z. Cao, T. Li, J. Mater. Sci. Technol. 33 (7) (2017) 712–717.
[35] C. Ai, F. He, M. Guo, J. Zhou, Z. Wang, Z. Yuan, Y. Guo, Y. Liu, L. Liu, J. Alloys Compd. 735 (2018) 2653–2662.
[36] B. Chanda, J. Das, Adv. Eng. Mater. 20 (4) (2018).
[37] W. Huo, H. Zhou, F. Fang, X. Zhou, Z. Xie, J. Jiang, J. Alloys Compd. 735 (2018) 897–904.
[38] T. Xie, Z. Xiong, Z. Xu, X. Cheng, Mater. Sci. Eng.: A 786 (2020).
[39] L. Jiang, Z.Q. Cao, J.C. Jie, J.J. Zhang, Y.P. Lu, T.M. Wang, T.J. Li, J. Alloys Compd. (2015).
[40] H. Jiang, H. Zhang, T. Huang, Y. Lu, T. Wang, T. Li, Mater. Des. 109 (2016) 539–546.
[41] Y. Yin, D. Kent, Q. Tan, M. Bermingham, M.-X. Zhang, J. Mater. Sci. Technol. 51 (2020) 173–179.
[42] Q. Shen, X. Kong, X. Chen, J. Mater. Sci. Technol. 74 (2021) 136–142.
[43] I. Basu, V. Ocelík, J.T.D. Hosson, Acta Mater. 157 (2018) 83–95.
[44] I. Basu, J.T.M.D. Hosson, Scr. Mater. 187 (2020) 148–156.
[45] J. Joseph, T. Jarvis, X. Wu, N. Stanford, P. Hodgson, D.M. Fabijanic, Mater. Sci. Eng. A 633 (2015) 184–193.
[46] H.R. Sistla, J.W. Newkirk, F.F. Liou, Mater. Des. 81 (2015) 113–121.